Jurnal Kejuruteraan 38(1) 2026: 289-300
https://doi.org/10.17576/jkukm-2026-38(1)-26

Miniaturization of High Sensitivity Defected Ground Structure Based Microwave Sensor for Material Characterization

Mohamad Harris Misran[a*], Maizatul Alice Meor Said[a], Mohd Azlishah Othman[a], Noor Azwan Shairi[a], Zahriladha Zakaria[a], Abd Majid Darsono[a], Suleiman Aliyu Babale[b] & Mohd Zahid Idris[c]

[a]*Centre for Telecommunication Research & Innovation (CeTRI), Fakulti Teknologi dan Kejuruteraan Elektronik dan Komputer (FTKEK), Universiti Teknikal Malaysia Melaka (UTeM), Hang Tuah Jaya, 76100, Durian Tunggal, Melaka, Malaysia.*

[b]*Department of Electronics and Telecommunications Engineering, Ahmadu Bello University, Zaria, Kaduna State, Nigeria*

[c]*Marine Engineering and ETO, Abu Dhabi Maritime Academy, 6th Streeet, Musaffah M-14, Abu Dhabi, United Arab Emirates*

[*]*Corresponding author: harris@utem.edu.my*

Received 16 May 2025, Received in revised form 1 September 2025
Accepted 1 October 2025, Available online 30 January 2026

ABSTRACT

One of the primary challenges in the advancement of microwave sensor technology lies in achieving an optimal balance between miniaturization and operational performance. Miniaturization often leads to a reduction in sensitivity and measurement accuracy, thereby limiting the practical applicability of compact microwave sensors. To address this issue, this study proposes the development of a high-precision microwave sensor based on a Defected Ground Structure (DGS), fabricated on a 1.6 mm-thick FR-4 substrate. The sensor design incorporates a 2-Ring Square Split Ring Resonator (SSRR) embedded within the DGS configuration to enhance electromagnetic field confinement and improve sensing capabilities. The sensor's performance was systematically evaluated by examining the effect of dimensional scaling on its sensitivity. In particular, variations in the resonant frequency of the transmission coefficient (S_{21}) were analyzed as a function of sensor size reduction. Through an extensive optimization process, the sensor's physical footprint was successfully reduced by 58%, without compromising the integrity of the DGS architecture. Prior to miniaturization, the sensor demonstrated an accuracy of approximately 81%. Following the size reduction, accuracy markedly improved to 98%, representing a significant enhancement in detection capabilities. This improvement is primarily attributed to the optimization of the surface current distribution intensity, which resulted in stronger localized electromagnetic fields and heightened responsiveness to minor perturbations in the sensor's environment. Thus, the optimized miniaturized sensor presents a promising solution for high-precision, compact microwave sensing applications, maintaining high sensitivity and reliability despite a substantial decrease in physical dimensions.

Keywords: High sensitivity; high accuracy; microwave sensor; Defected Ground Structure; Split Ring Resonator; miniaturization

INTRODUCTION

Microwave sensors have become one of the preferred choices for various applications, including leak detection, due to their ability to detect subtle changes in the environment (Talhah Mohamad Shirajuddina et al. 2022). Unlike fiber optic sensors that use light waves to transmit data, microwave sensors operate by emitting electromagnetic waves, which are then reflected back to the sensor, allowing them to detect changes in the surrounding area (Nur Shufinah Suhaimia et al. 2024).

The permittivity of a material significantly influences how it interacts with electromagnetic (EM) waves, making its precise characterization a fundamental requirement in microwave engineering. Accurate permittivity measurements are essential for various applications, including antenna design, microwave circuit optimization,

and non-destructive evaluation techniques in which dielectric properties govern system behavior and signal propagation (Özkal & Yaman 2023).

Dielectric measurement methodologies can be broadly classified into resonant and non-resonant approaches, each implemented through either reflection or transmission modes. Non-resonant techniques, in particular, determine the permittivity of materials by observing the variation in electromagnetic wave characteristics such as impedance and propagation velocity via transmission and reflection coefficients (Kiani, Rezaei & Fakhr 2021). These techniques are advantageous in their simplicity and wide frequency range but often lack the high sensitivity provided by resonant systems.

In recent years, growing interest has been shown in applying Defected Ground Structure (DGS) in microwave component design, particularly for sensor miniaturization. DGS involves etching specific patterns onto the ground plane of a microstrip, thereby disrupting surface current distribution and altering the EM properties of the transmission line (Gangwar, Pathak & Kumar 2023). This disruption results in improved characteristics, including the ability to produce stopband behavior and induce slow-wave effects, both of which are critical in enhancing sensor resolution and compactness (Dokmetas et al. 2021).

The conceptual origin of DGS traces back to the development of photonic bandgap (PBG) structures in optical systems, which were initially explored for controlling the propagation of light waves. The transition of this concept into the microwave domain led to the emergence of DGS as an effective means to manipulate microwave signals with greater precision and in reduced geometrical footprints (Gangwar et al. 2023).

Despite their advantages, resonant perturbation techniques traditionally depend on large, expensive cavity structures like waveguide resonators to achieve high sensitivity and accurate dielectric characterization. These structures, while effective, are often impractical for compact, cost-sensitive applications due to their bulk and manufacturing complexity (Hocini, Ben Salah & Temmar 2021).

To mitigate these limitations, researchers have turned to metamaterial-inspired resonators, particularly the Complementary Split Ring Resonator (CSRR), which exhibits negative effective permittivity within a specific frequency band. CSRR-based sensors offer a compact alternative that enables high sensitivity measurements in a planar format (Alotaibi, Cui, & Tentzeris, 2019). These structures serve as the electromagnetic dual of conventional Split Ring Resonators (SRRs) and are capable of producing strong localized fields, thus making them highly responsive to dielectric perturbations (Shahzad et al. 2022).

Recent investigations into CSRR designs have led to the development of both single-ring and double-ring configurations, each with unique sensitivity characteristics. However, comprehensive studies comparing their sensitivity performance remain limited, especially in the context of material characterization at low concentrations (Saadat-Safa et al. 2019). As such, there is a growing need to explore optimized configurations that enhance both sensitivity and selectivity for trace-level detection.

Planar microwave resonator-based sensors have gained substantial traction due to their suitability for integration into modern electronic systems and their ability to operate in one-port or two-port configurations. These designs have been widely employed for applications such as chemical and biological sensing, where they enable permittivity extraction of both solid and liquid analytes (Alahnomi et al. 2021).

Nevertheless, challenges persist in improving the selectivity and sensitivity of these sensors, particularly in the detection of low-permittivity substances or analytes present in very low concentrations (parts per million or less). Recent sensor designs, although effective in general applications, often struggle to offer the level of precision demanded in critical industrial and biomedical environments (Roslan et al. 2022).

To address this gap, advanced metamaterial-based designs like dual-band or multi-resonance resonators have been introduced, offering greater detection range and material discrimination. However, the sensitivity thresholds of many of these systems still require refinement to meet the rigorous demands of real-world sensing environments (Moradpour & Zarifi 2023). By integrating DGS and CSRR, the field confinement around the sensing region, which directly influences sensitivity to material changes is improved and particularly useful for accurate material characterization in compact applications (Amer et al. 2025)

The proposed sensor is designed to detect changes in dielectric properties by monitoring shifts in its resonant frequency. The principle is that when a Material Under Test (MUT) with varying dielectric constants is introduced onto the resonant structure, specifically over areas of high surface current density, the resultant perturbation causes a measurable shift in the transmission coefficient resonance (Al-Behadili et al. 2021). A high sensitivity reading is obtained when small changes in the dielectric constant lead to large frequency shifts, demonstrating the sensor's ability to detect minor variations in material properties with high precision (Misran et al. 2024).

This study will focus on integration of DGS and optimized resonator structures in a compact planar format to offer a promising path forward for the development of cost-effective, high-performance microwave sensors. Such designs are particularly relevant for applications requiring accurate permittivity characterization in compact, portable, or embedded systems.

METHODOLOGY

In the context of microwave sensor design, the adoption of a two-port configuration offers several critical advantages over the conventional single-port approach. A two-port system enables simultaneous measurement of both transmission coefficient S_{21} and reflection coefficient S_{11} parameters, thereby providing a more comprehensive characterization of the sensor's electromagnetic behavior. The availability of S_{21} enhances the ability to detect subtle variations in resonant frequency and amplitude, leading to improved sensitivity and higher measurement resolution. Furthermore, two-port configurations inherently reduce the influence of impedance mismatch and parasitic reflections, which are common limitations in single-port systems, thus ensuring greater measurement stability and repeatability.

From a practical perspective, two-port sensors demonstrate enhanced resilience against environmental noise and system-induced interferences, owing to the defined signal propagation path from input to output. This characteristic also facilitates the implementation of differential measurement techniques, further improving the system's ability to discern minute perturbations in the surrounding environment. Consequently, the two-port architecture presents a superior platform for the development of high-precision, high-sensitivity microwave sensors, particularly in applications where accuracy, robustness, and reliability are of paramount importance.

The flowchart in Figure 1 outlines the systematic process for designing and evaluating a microwave sensor. The initial step involves specifying the sensor parameters, such as material and operating frequency, based on microwave sensor theory. This is followed by a simulation design phase utilizing CST, integration of DGS into design, aimed at enhancing the sensor's performance. The optimization phase ensures that the design conforms to the specified requirements, adjusting parameters for optimal performance.

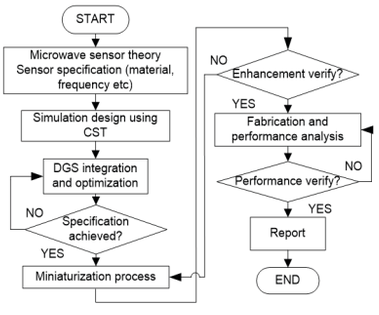

FIGURE 1. Design of the microwave sensor

Miniaturization process is done to enhance the performance of the sensor. The performance verification through experimental analysis validates the sensor's functionality and compares it with simulation results. Analysis is conducted to evaluate the sensor's real-world behavior and performance against theoretical predictions.

The sensor design is initiated with a base structure measuring 100mm × 50mm, incorporating a single microstrip line along with a full ground plane. This initial configuration serves as a benchmark for testing different DGS integrated into the ground plane to optimize sensor performance. Figure 1(a) shows the front view of microstripline for the proposed sensor.

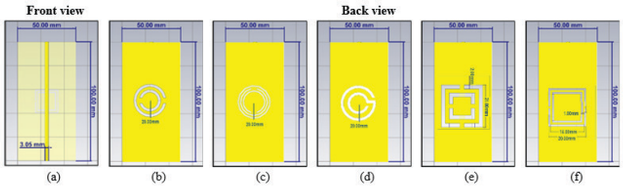

FIGURE 2. Design of the microwave sensor

To explore the impact of a more complex DGS, Figure 2(b) and Figure 2(c) present a back view design with 2 rings and 3 rings of SRR, respectively, offering insights into how the addition of another resonant element influences the sensor's sensitivity and bandwidth. This design helps assess the scalability of CSRR structures and their ability to improve performance in terms of frequency selectivity and impedance matching. Figure 2(d) introduces a circular G-shaped SRR into the design, aiming to investigate the role of coil-based geometries as a DGS. The circular G-SRR provides an opportunity to study the interaction between the sensor and the material under test, with particular emphasis on the impact of coil structures on electromagnetic field enhancement and frequency shifts.

Further examination is provided in Figure 2(e) and Figure 2(f), where 2 ring SRRs with gap sizes of 2mm and 1mm are implemented, respectively. These designs allow for the examination of how gap dimensions in the SRR structure influence the sensor's resonance behaviour and overall performance. The analysis of these different DGS configurations is critical in understanding their impact on sensor performance, particularly in terms of frequency response, impedance matching, and the sensitivity of the sensor to material property variations. The performance of each antenna design is carefully observed and analyzed, with results contributing to the overall optimization of the sensor's design for practical applications.

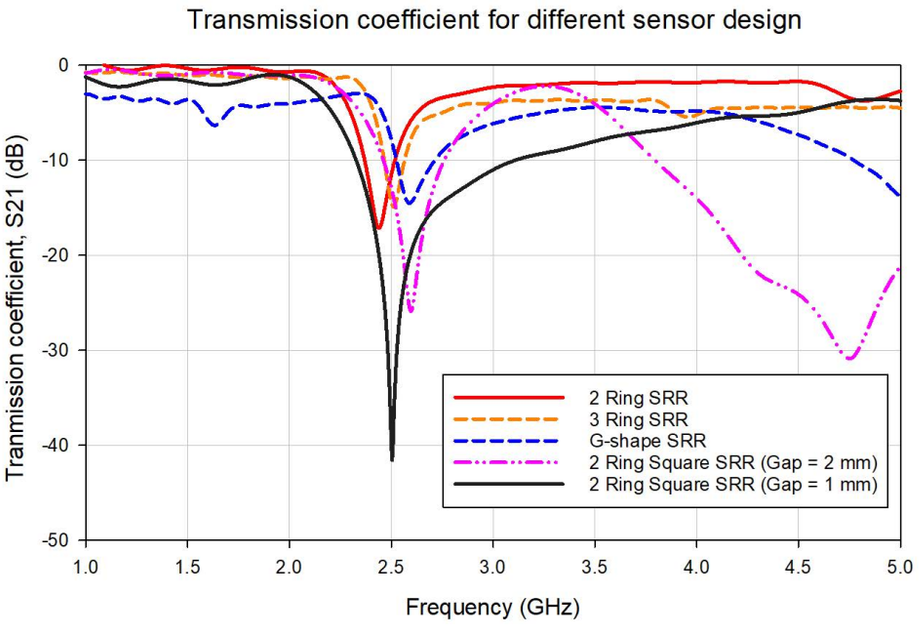

FIGURE 3. S-parameter performance comparison of various sensor design

Figure 3 illustrates the relationship between the resonance frequency and dielectric constant of a sensor. All of the DGS designs investigated are capable of producing resonant frequencies with an S_{21} magnitude lower than -10 dB, demonstrating effective signal attenuation and resonance behaviour. This implies that the sensor can exhibit significant electromagnetic interaction with the material under test, leading to efficient detection of changes in material properties. Among the different DGS configurations tested, the sensor with the SSRR featuring a 1mm gap achieved the best performance, reaching a resonant frequency of -41.576 dB at 2.5 GHz. This sharp resonance is reflected by a narrow and deep dip in the S21 curve, ensuring a high Q-factor, which is crucial for enhancing the sensor's sensitivity and selectivity. The high Q-factor indicates that the sensor has a narrow resonance bandwidth, allowing it to detect subtle variations in the material properties with higher precision and improved signal-to-noise ratio.

The square ring DGS performs better than the circular ring DGS due to several key factors related to the electromagnetic behaviour of the structures. A square ring creates sharper corners and edges compared to a circular ring, which allows for a more concentrated electromagnetic field at the corners. These areas with higher field intensity can lead to more effective coupling between the resonator and the material under test, improving the overall sensor performance.

The gap size in SRRs results in stronger coupling between the resonant rings, leading to enhanced electromagnetic interaction and the sensor's sensitivity to changes in the dielectric properties of the material under test.

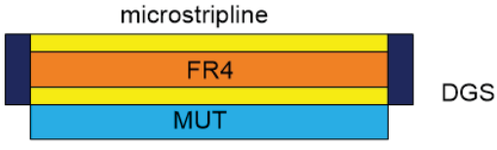

FIGURE 4. MUT position on the sensor

The MUT was simulated and designed on the DGS design to investigate the effect of varying dielectric constants to the resonant frequency as shown in Figure 4. The dielectric constant of the MUT varied between 1 and 6, and the S_{21} parameter was measured to analyze the changes in frequency response. This range is chosen because the dielectric constant of the measured MUTs are within this range value.

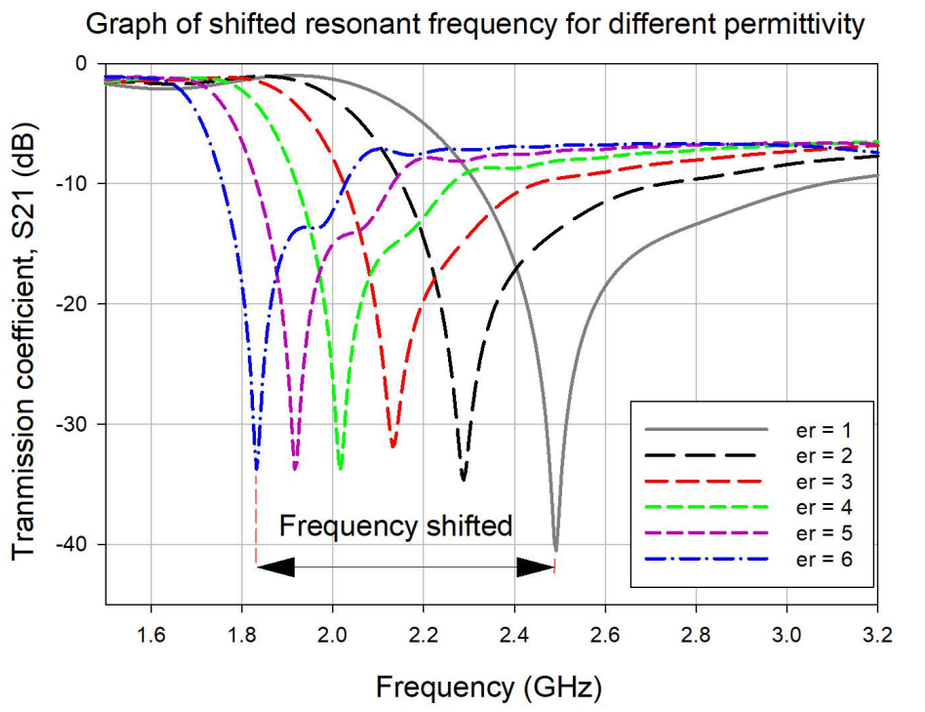

FIGURE 5. Resonant frequency for 2 ring SSRR with different MUT's dielectric constant

TABLE 1. Comparison of different sensor design

DGS Design	Frequency Shift	(dB)	Sensitivity
2 Rings-SRR	2.5 GHz to the 1.9 GHz 600 MHz difference	-16.6917 dB at 2.5 GHz	120
3 Rings-SRR	2.5 GHz to the 1.86 GHz 640 MHz difference	-13.8745 dB at 2.5 GHz	128
G-Shape SRR	2.58 GHz to the 2.08 GHz 500 MHz difference	-14.3756 dB at 2.58 GHz	10
2 Ring SSRR (Gap = 2 mm)	2.6 GHz to the 2.005 GHz 595 MHz difference	-26.8067 dB at 2.6 GHz	119
2 Ring SSRR (Gap = 1 mm)	2.5 GHz to the 1.832 GHz 668 MHz difference	-41.576 dB at 2.5 GHz	133.6

a Frequency shifted when dielectric constant varied from 1 to 6

Referring to Figure 5, the dielectric constant of a material significantly impacts the propagation of electromagnetic waves, affecting the resonant frequency of the structure. As the dielectric constant of the MUT increased, the resonant frequency shifted. This shift occurs because materials with higher dielectric constants have greater ability to store and transfer electromagnetic energy, which slows down the electromagnetic waves traveling through the material. This step is repeated with each design to observe the sensor performance.

Table 1 summarizes the shifted frequency when the MUT with 1 to 6 dielectric constants was placed on each sensor. From the data, the sensor with the 2-ring SSRR DGS design exhibited the largest frequency shift as the dielectric constant varied, indicating the high sensitivity of this sensor. As a result, this sensor was selected as the final design.

The sensitivity of the sensor can be calculated by:

$$Sensitivity, S = \frac{\Delta f}{\Delta er'} \quad (1)$$

Sensor then miniaturized and the performance was simulated. The decision to miniaturize a microwave sensor from 100x50 mm to 70x30 mm is influenced by a combination of theoretical and practical factors. The benefit of reducing the sensor size is the potential for improved resolution. A smaller sensor often leads to better spatial resolution, enhancing the precision of measurements, particularly when analyzing small-scale materials or intricate details. However, miniaturization presents trade-offs, as overly small sensors may suffer from reduced signal strength or sensitivity. The chosen 70x30 mm size

represents an optimal balance, offering sufficient compactness while maintaining high performance in terms of beamwidth, sensitivity, and measurement accuracy. This size effectively balances sensor performance constraints and ensures that the sensor remains efficient without compromising the measurement quality of the MUT.

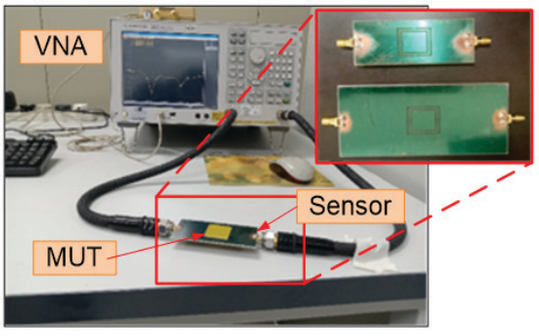

FIGURE 6. Measurement setup using VNA

Fabricated antenna, as shown in Figure 6 is measured and analyzed. This measurement process includes several equipment which is the Vector Network Analyzer (VNA) that connected to the proposed sensor through cable with 50 ohms SMA. The MUTs selected for measurement stage is FR4 with ε_r of 4.3, FR4 with ε_r = 5.4, and Roger Duroid with ε_r = 2.2.

The MUT is strategically positioned over the DGS, specifically covering the SSR region, where the surface current density is maximized; as this area is most sensitive to perturbations, any alteration; such as varying dielectric constants; directly influences the resonant frequency, thereby enabling the sensor to distinguish between different materials based on their dielectric properties.

RESULTS AND DISCUSSION

The rate of resonant frequency change as a function of various dielectric constants and loss tangents was analyzed and plotted on a graph to gain a deeper understanding of how these material properties influence the sensor's response.

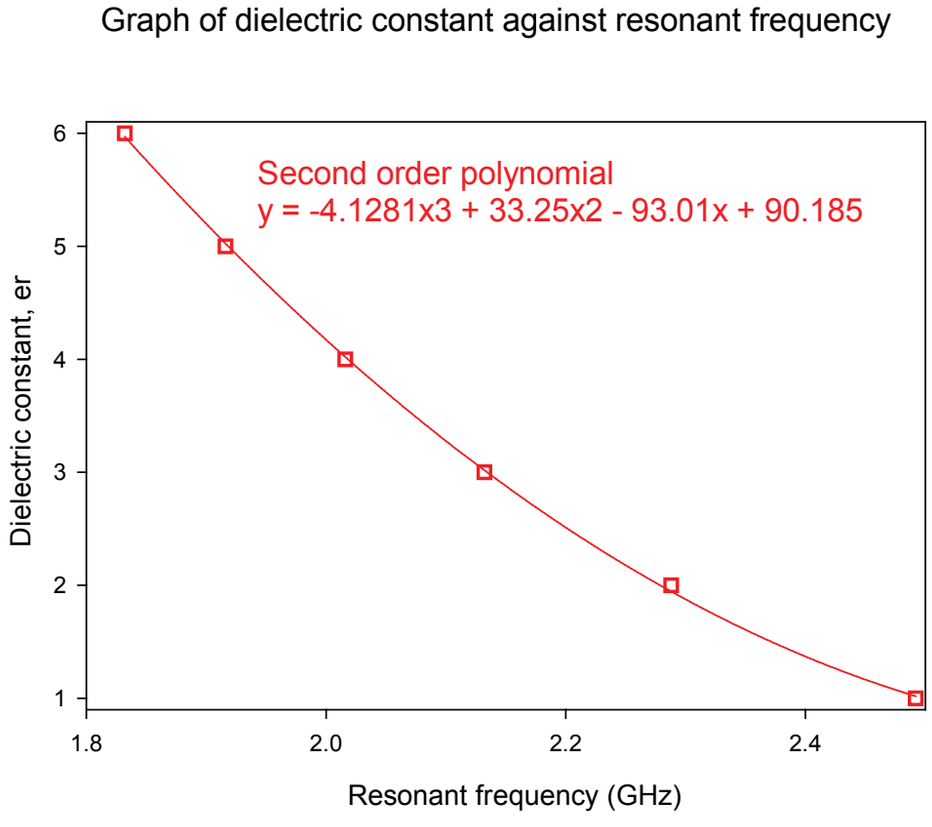

FIGURE 7. S- Frequency shifting with different dielectric constants, εr

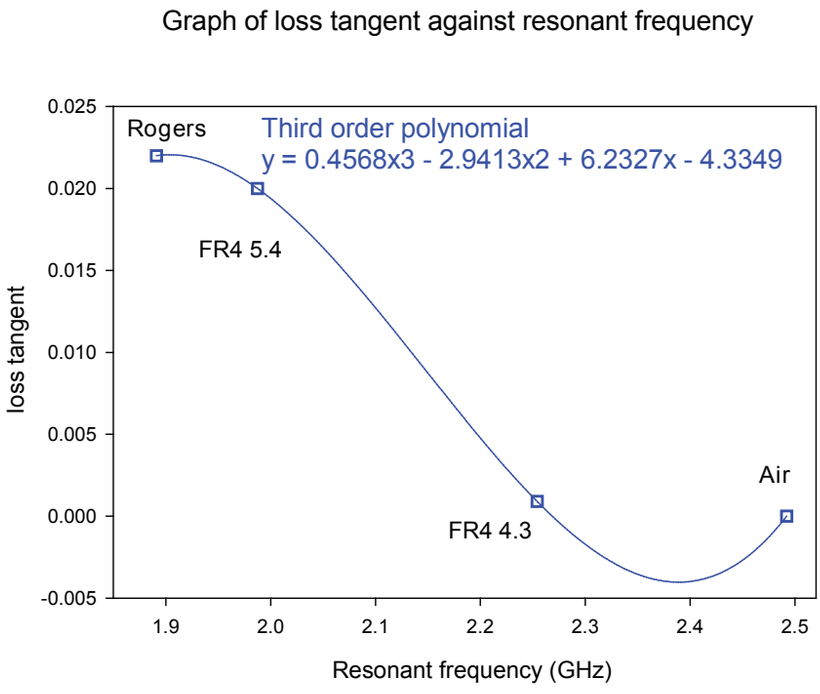

FIGURE 8. S- Frequency shifting with different loss tangent

This approach allows for a quantitative interpretation of the relationship between the resonant frequency shift and the dielectric properties of the MUT. By plotting this data, researchers can accurately predict how changes in the MUT's dielectric constant and loss tangent will affect the resonant frequency, which is crucial for sensor calibration and accurate measurements.

The graph, as shown in Figures 7 and 8, demonstrates a clear relationship between the resonant frequency and both the dielectric constant and loss tangent. This relationship can be modeled using a polynomial equation, which provides a robust framework for understanding the complex interactions between the sensor's electromagnetic waves and the MUT's dielectric properties. The polynomial model captures the non-linear nature of the frequency shift and offers a more precise prediction of the resonant frequency change when applied to materials with varying dielectric constants and loss tangents.

One of the notable aspects of this analysis is that the reference graph and its polynomial model are applicable to both normal sensors and miniaturized sensors. This is due to the fact that both sensor types exhibit similar S_{21} characteristics based on simulation results

The general form of this second order polynomial equation is provided in Equation (2). Similarly, the relationship between resonant frequency and the MUT's loss tangent is best described by a third-order polynomial equation, which is shown in Equation (3). These polynomial equations were derived from the graph and will be used to calculate the measured values of the MUT's material characteristics with high accuracy.

$$y = Ax^2 + Bx + C \tag{2}$$

$$y = Ax^3 + Bx^2 + Cx + D \tag{3}$$

The Q-factor of the sensor can be determined using equation (4).

$$Q - factor = \frac{2f_o}{BW} \tag{4}$$

The MUT was strategically placed on top of the Defected Ground Structure (DGS), a configuration known for its ability to concentrate electromagnetic fields in specific localized regions. The etched defect in the ground plane disrupts the current flow, resulting in an intensified surface current density around the defect area. This increased current distribution density enhances the electromagnetic interaction between the sensor and the MUT. As a result, even small changes in the dielectric properties of the MUT lead to significant perturbations in the resonant frequency, thereby improving the sensor's overall sensitivity and detection accuracy for material characterization.

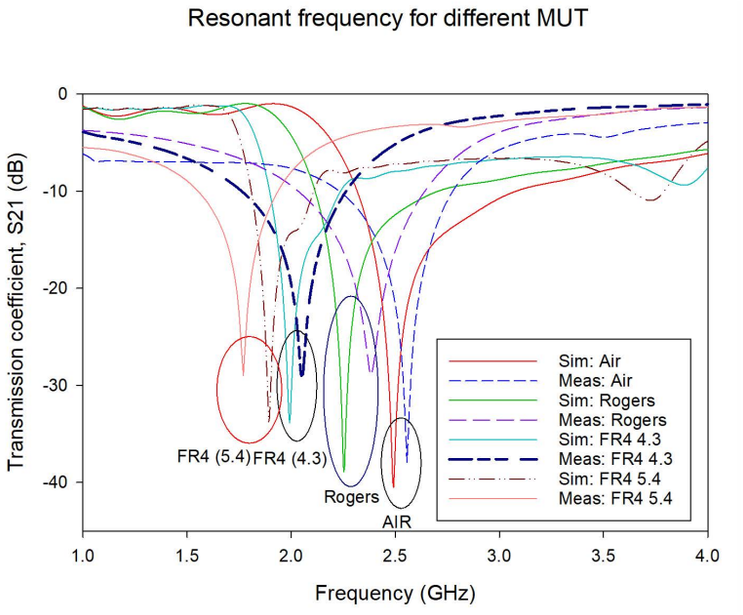

FIGURE 9. Graph of resonant frequency for 100x50 mm sensor

Figure 9 and Figure 10 present the comparison between the simulated S_{21} values and the measured S_{21} values, illustrating the correlation between the simulation predictions and the actual experimental results for both the 100 x 50 mm sensor and the miniaturized sensor, respectively. This comparison plays a crucial role in validating the effectiveness of the proposed model and confirming the accuracy of the sensor's response. In the measurement process, three different MUTs were used to assess the sensor's performance and verify the simulation results. The MUTs selected for this evaluation include FR4 with ε_r of 4.3, FR4 with $\varepsilon_r = 5.4$, and Roger Duroid with $\varepsilon_r = 2.2$, which are commonly used in the industry for sensor testing.

As shown in Figure 9, the measurements of the larger sensor (100 x 50 mm) display a significant deviation when compared to the simulated results. The size of the sensor relative to the MUT significantly affects measurement accuracy. A large sensor results in a lower sensor to MUT ratio, which means the sensor covers a broader area, potentially missing fine details or localized variations in the MUT. This often leads to a discrepancy between simulation and measurement results. Simulations typically assume ideal interactions, while larger sensors may average out important nuances, causing inaccuracies. Conversely, a smaller sensor offers a higher sensor to MUT ratio, capturing more precise and localized measurements, leading to better alignment between simulation and actual measurement results.

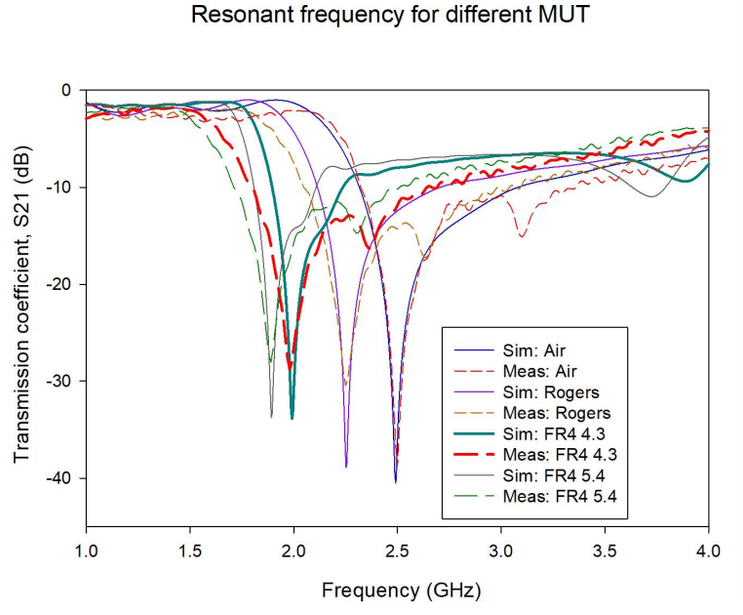

FIGURE 10. Graph of resonant frequency for miniaturized (70x30 mm) sensor

In contrast, Figure 10 demonstrates that the measurements for the miniaturized sensor are much closer to the simulated predictions, with only negligible differences observed. This indicates that the miniaturized sensor's performance aligns more accurately with the simulation, likely due to its more controlled electromagnetic characteristics and reduced sensitivity to external factors. The minimal deviation between measurement and simulation for the miniaturized sensor further validates the accuracy of the model and its applicability to smaller sensor designs. The results highlight the effectiveness of the proposed sensor model and offer confidence in its ability to accurately predict sensor performance, especially for more compact sensor configurations.

The resonant frequency measured for each MUT was utilized in the derived polynomial equations to determine the dielectric constant and loss tangent of the material. The second-order polynomial equation was applied for the relationship between the resonant frequency and dielectric constant, while the third-order polynomial equation was used to relate the resonant frequency with the loss tangent. These equations allowed accurate characterization of the MUT's properties, ensuring a reliable analysis of its performance. The measured resonant frequency obtained from the transmission response is then substituted into the analytical second and third order polynomial equation derived from the resonator model to calculate the effective permittivity of the MUT.

The measured data were systematically recorded and analyzed to evaluate the sensor's effectiveness in detecting variations in material properties. This analysis provided critical insights into the sensor's sensitivity and its ability to differentiate between materials with varying dielectric constants and loss tangents for both sensors. Table 2 summarizes the performance of the initial sensor and the miniaturized antenna.

TABLE 2. Comparison of sensor performance

Type of Sensor		*mini*	large	*mini*	large	*mini*	large	*mini*	large
MUT		*Air*	Air	*FR4 (4.3)*	FR4 (4.3)	*FR4 (5.4)*	FR4 (5.4)	*Rogers*	Rogers
Simulation (GHz)		*2.5*	2.5	*2.28*	2.28	*2.02*	2.02	*1.91*	1.91
Measurement (GHz)		*2.49*	2.557	*2.25*	2.39	*1.99*	2.05	*1.88*	1.69
Shifted Freq (MHz)		*NA*	NA	*240*	110	*500*	30	*610*	220
Dielectric Constant	Reference	*1*	1	*4.3*	4.3	*5.4*	5.4	*2.2*	2.2
	Measured	*1.02*	0.85	*4.27*	7.77	*5.41*	3.71	*2.18*	1.41
Accuracy (%)		*97.4*	85.48	*98.98*	19.30	*99.28*	68.70	*99.66*	64.09
Loss Tangent	Reference	*0*	0	*0.0009*	0.022	*0.02*	0.02	*0.022*	0.0009
	Measured	*0.0003*	0.0080	*0.0001*	0.0026	*0.0202*	0.0167	*0.0221*	0.00355
Accuracy (%)		*NA*	NA	*88.89*	11.82	*99*	83.55	*99.55*	0
Q-Factor		*595*	255.7	*234*	95.6	*259.1*	82	*393.8*	84.5
Sensitivity (MHz/εr)		*NA*	NA	*200*	33.33	*151.5*	6.81	*138.6*	183.3

The table is divided into two sections, one column represents the miniaturized sensor with a reduced size, while the other column corresponds to the initial 100 × 50 mm sensor. The performance comparison highlights the advantages between the compact design and the original, emphasizing the impact of miniaturization on sensitivity and accuracy.

The measured S_{21} for the miniaturized sensor closely matches the simulation results, validating its performance and confirming the sensor's reliability for practical applications. This alignment between measured and simulated data demonstrates that the miniaturized sensor is highly accurate in characterizing the dielectric properties of the MUT. On the other hand, the larger sensor exhibited significant deviations between simulation and measurement, leading to inaccurate characterization of the MUT. These discrepancies result in less reliable data, undermining the sensor's ability to provide precise material property measurements.

In terms of accuracy, the large sensor's performance varied significantly, with accuracy ranging from 19.3% to 85.48%. In contrast, the miniaturized sensor consistently delivered precise readings, with accuracy fluctuating between 97.4% and 99.66%. This demonstrates a substantial improvement in terms of accuracy, with the miniaturized sensor offering more reliable and consistent results. Furthermore, the miniaturized sensor was able to determine the dielectric constant and loss tangent of the MUT with minimal deviation, ensuring accurate material characterization across a wide range of samples.

The miniaturized sensor also exhibited a significantly higher Q-factor, reaching values up to 595, compared to the average Q-factor of 90 observed in the large sensor. This significant enhancement in the Q factor indicates that the miniaturized sensor can achieve sharper resonance and better performance in terms of signal sensitivity and frequency resolution. Additionally, the miniaturized sensor demonstrated improved sensitivity, with a frequency shift range of 138.6 to 200 MHz/εr, compared to the large sensor, which had a frequency shift range of 6.8 to 183 MHz/εr.

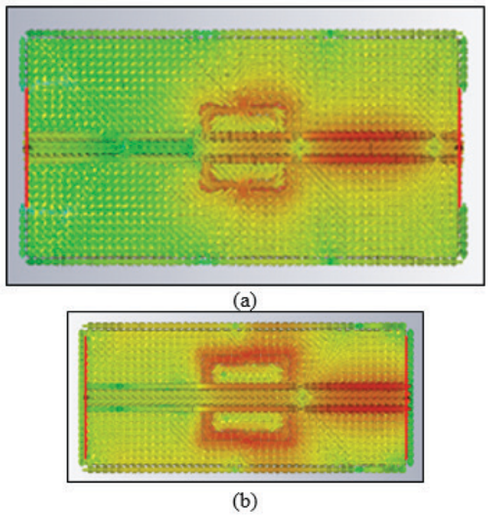

FIGURE 11. Surface current distribution between (a) 100 x 50 mm (b) 70 x 30 mm sensor

Figure 11(a) illustrates a sensor with significantly lower surface current density when compared to the miniaturized sensor depicted in Figure 11(b). This variation is primarily attributed to the difference in the physical dimensions of the two sensor configurations. In Figure 11(b), the sensor has going through a miniaturization process, which results in a reduced structural footprint.

The reduction in size of microwave sensors leads to a more confined spatial distribution of electromagnetic fields due to the increased interaction between the fields and the sensor's material boundaries. As the sensor shrinks, the electromagnetic waves become more confined within the small structures, such as microstrip lines or resonators, which intensify the electric field in these regions. This phenomenon results from the electromagnetic field's tendency to concentrate in areas of high impedance, typically occurring in miniaturized designs. Consequently, the sensor's sensitivity may improve, but it also requires careful optimization to manage field distribution and avoid unwanted parasitic effects (Abdolrazzaghi et al. 2022).

The increase in surface current density plays a critical role in enhancing the sensor's performance. Specifically, higher current density leads to stronger electromagnetic interactions with the surrounding material, which translates into greater sensitivity. This enhanced sensitivity allows the miniaturized sensor to detect even smaller variations in the dielectric properties of the MUT, making it more effective for precision sensing applications. In contrast, the larger sensor shown in Figure 9(a) displays a more distributed field pattern due to its extended area. This wider distribution leads to a lower concentration of energy and thus a reduced surface current density. As a result, the sensitivity of the larger sensor is diminished, limiting its effectiveness in applications where high precision and responsiveness to subtle environmental changes are required.

TABLE 3. Comparison of proposed sensor's performance

Sensor	Accuracy %	Q- factor	Sensitivity MHz/ε_r	Substrate of Sensor	Type of sensors
Al-Gburi et al, 2023	99.72	520	77.39	Rogers	Triple Rings CSRR
Kunal et al, 2024	97 - 99	NR	129.4	Rogers	Triple Ring Bridge CSRR
Akash et al, 2024	98.85	NR	246.48	FR4	Hexagonal Split Ring Resonator
This work	99.28	595	200	FR4	Miniaturized SSRR DGS

Planar microwave sensors, despite extensive academic research, face limited industrial adoption due to challenges like lower sensitivity, environmental sensitivity, and integration difficulties. Although they offer compactness and potential for low-cost fabrication, they are not widely available in the market.

The proposed sensor demonstrates several key advantages over the others sensor design listed in Table 3. One notable benefit is its lower percentage error, with a value of 0.72%, which is significantly lower than the other sensors, such as Triple Ring Bridge CSRR sensor with 3% (Kunal et al, 2024) and Hexagonal Split Ring Resonator sensor with 1.15% (Akash et al, 2024). This reduced percentage error indicates superior accuracy, making the proposed sensor more suitable for high-precision applications. Additionally, the proposed sensor exhibits a high Q-factor of 595, surpassing the Q-factors of sensors such as Triple Rings CSRR sensor with 520 (Al-Gburi et

al, 2023). A higher Q-factor corresponds to improved energy storage and selectivity, contributing to enhanced performance in sensing and filtering applications. The sensitivity of the proposed sensor also outperforms others with 200 MHz/ε_r. This characteristic will ensure the selectivity and the capability of the sensor to differentiate small variation of dielectric constant in MUT.

CONCLUSION

In conclusion, the miniaturized sensor outperforms the larger sensor in multiple aspects, including accuracy, sensitivity, Q-factor, and overall performance. The ability to achieve precise measurements of dielectric constant and loss tangent, combined with higher sensitivity and a significantly enhanced Q-factor, makes the miniaturized sensor as a more effective tool for material characterization. These findings highlight the advantages of miniaturizing sensor designs, offering a compact solution without compromising performance, and suggest that the miniaturized sensor is better suited for applications requiring high precision and reliability in material property measurements.

ACKNOWLEDGEMENT

The author would like to thank the Fakulti Teknologi dan Kejuruteraan Elektronik dan Komputer (FTKEK), Centre for Research and Innovation Management (CRIM) and Universiti Teknikal Malaysia Melaka (UTeM) for financing this work.

DECLARATION OF COMPETING INTEREST

None.

REFERENCES

Abdulkarim, Y. I., Al-Gburi, A. J. A., Zakaria, Z., Rahman, N. A., Althuwayb, A. A., Ibrahim, I. M., Saeidi, T., Dayo, Z. A., & Ahmad, S. 2023. A miniaturized and highly sensitive microwave sensor based on CSRR for characterization of liquid materials. *Materials* 16(9): 3416.

Abdolrazzaghi, M., Nayyeri, V., & Martín, F. 2022. Techniques to improve the performance of planar microwave sensors: A review and recent developments. *Sensors* 22(18): 6946.

Al-Behadili, A. A., Zakaria, Z., Khalily, M., Althuwayb, A. A., & Tiong, S. K. 2021. Differential microstrip sensor for complex permittivity characterization of organic fluid mixtures. *Sensors* 21(23): 7865.

Alahnomi, R. A., Zakaria, Z., Yusof, N. M., Hamzah, M. H., Masuri, N. A., & Ghadiri, M. 2021. Review of recent microwave planar resonator-based sensors: Techniques of complex permittivity extraction, applications, open challenges and future research directions. *Sensors* 21(7): 2267.

Alotaibi, S. A., Cui, Y., & Tentzeris, M. M. 2019. CSRR-based sensors for relative permittivity measurement with improved and uniform sensitivity throughout 0.9–10.9 GHz band. *IEEE Sensors Journal* 20(9): 4667–4678.

Amer, A. B. A., Shairi, N. A., Meor Said, M. A., Zakaria, Z., Misran, M. H., Othman, A., Alam, S., & Abdul Rahim, S. K. 2025. Single-port microwave sensor using defected ground structure complementary split ring resonator for solid material characterization. *Progress In Electromagnetics Research C* 158: 139–149.

Buragohain, A., Das, G. S., Beria, Y., Al-Gburi, A. J. A., Kalita, P. P., & Doloi, T. 2023. Highly sensitive differential hexagonal split ring resonator sensor for material characterization. *Sensors and Actuators A: Physical* 363: 114704.

Dokmetas, B., Öztürk, M., Karaaslan, M., Akgol, O., Sabah, C., & Bhatti, G. 2021. A compact bandstop filter design using DMS–DGS technique for radar applications. *The Applied Computational Electromagnetics Society Journal (ACES)* 36(12): 1460–1467.

Gangwar, R. K., Pathak, A. K., & Kumar, S. 2023. Recent progress in photonic crystal devices and their applications: A review. *Photonics* 10(11): 1205.

Hocini, A., Ben Salah, H., & Temmar, M. N. 2021. Ultra-high-sensitive sensor based on a metal–insulator–metal waveguide coupled with cross cavity. *Journal of Computational Electronics* 20(3): 1354–1362.

Kiani, S., Rezaei, P., & Fakhr, M. 2021. An overview of interdigitated microwave resonance sensors for liquid samples permittivity detection. In *Interdigital sensors: Progress Over The Last Two Decades*, pp. 153–197.

Misran, M. H., Said, M. A. M., Othman, M. A., Salleh, A., Suhaimi, S., & Idris, M. Z. 2024. High sensitivity double split ring resonator–defected ground structure (DSRR–DGS) based microwave sensors for material characterization. In *Proceedings of the 2024 IEEE Asia-Pacific Conference on Applied Electromagnetics (APACE 2024)*, pp. 440–443.

Moradpour, M., & Zarifi, M. H. 2023. High-resolution PEDOT: PSS-based planar microwave resonator sensor. *IEEE Sensors Journal* 23(18): 21216–21225.

Suhaimi, N. S., Meor Ahmad, M. I., Nuawi, M. Z., Zohari, M. H., Ariffin, A. K., & Abdullah, A. Z. M. 2024. Determination of train vehicle speed using fibre Bragg grating sensors for railway application. *Jurnal Kejuruteraan* 36(2): 758–792.

Özkal, C., & Yaman, F. 2023. A non-resonant approach for dielectric constant reconstructions via Newton iterations. *AEU – International Journal of Electronics and Communications* 170: 154802.

Roslan, H. S., Zakaria, Z., Rahman, N. A., Althuwayb, A. A., Ghadiri, M., & Hamzah, M. H. 2022. High sensitivity microwave sensor for material characterization using square split ring resonator. In *Proceedings of the 2022 IEEE International RF and Microwave Conference (RFM 2022)*, pp. 1–4.

Saadat-Safa, M., Khalaj-Amirhosseini, M., & Mirmozafari, M. J. 2019. A CSRR-based sensor for full characterization of magneto-dielectric materials. *IEEE Transactions on Microwave Theory and Techniques* 67(2): 806–814.

Shahzad, W., Khalid, S., Amin, Y., Kim, N., & Tentzeris, M. M. 2022. A low-cost metamaterial sensor based on DS-CSRR for material characterization applications. *Sensors* 22(5): 2000.

Singh, K. K., Singh, A. K., Mahto, S. K., Sinha, R., & Al-Gburi, A. J. A. 2024. Enhanced accuracy and high sensitivity in dielectric characterization through a compact and miniaturized metamaterial-inspired microwave sensor. *Sensors and Actuators A: Physical* 370: 115271.

Shirajuddin, T. M., Muhammad, N. S., & Abdullah, J. 2022. Systematic review on research trends on sensor-based leak detection methods in water distribution systems. *Jurnal Kejuruteraan* 34(2): 201–209.